

GALAXY CLUSTERS IN THE IRAC DARK FIELD II: MID-IR SOURCES

J.E. KRICK¹, J.A. SURACE¹, D. THOMPSON², M.L.N. ASHBY³, J.L. HORA³, V. GORJIAN⁴, AND L. YAN¹

Draft version October 29, 2018

ABSTRACT

We present infrared luminosities, star formation rates (SFR), colors, morphologies, locations, and AGN properties of $24\mu\text{m}$ -detected sources in photometrically detected high-redshift clusters in order to understand the impact of environment on star formation and AGN evolution in cluster galaxies. We use three newly-identified $z = 1$ clusters selected from the IRAC dark field; the deepest ever mid-IR survey with accompanying, 14 band multiwavelength data including deep *HST* imaging and deep wide-area *Spitzer* MIPS 24 micron imaging. We find 90 cluster members with MIPS detections within two virial radii of the cluster centers, of which 17 appear to have spectral energy distributions (SED) dominated by active galactic nuclei (AGN) and the rest dominated by star formation. We find that 43% of the star forming sample have infrared luminosities $L_{IR} > 10^{11}L_{\odot}$ (luminous infrared galaxies; LIRGs). The majority of sources (81%) are spirals or irregulars. A large fraction (at least 25%) show obvious signs of interactions. The MIPS -detected member galaxies have varied spatial distributions as compared to the MIPS-undetected members with one of the three clusters showing SF galaxies being preferentially located on the cluster outskirts, while the other 2 clusters show no such trend. Both the AGN fraction and the summed SFR of cluster galaxies increases from redshift zero to one, at a rate that is a few times faster in clusters than over the same redshift range in the field. Cluster environment does have an effect on the evolution of both AGN fraction and SFR from redshift one to the present, but does not effect the infrared luminosities or morphologies of the MIPS sample. Star formation happens in the same way regardless of environment making MIPS sources look the same in the cluster and field, however the cluster environment does encourage a more rapid evolution with time as compared to the field.

Subject headings: galaxies: clusters: individual — galaxies: evolution — galaxies: photometry — galaxies:active — infrared: galaxies — cosmology: observations

1. INTRODUCTION

Galaxy groups and clusters represent the dense environments required for hierarchical galaxy formation. Cluster galaxies potentially follow a different evolutionary path from isolated field galaxies because of a cluster's large gravitational potential and hot, X-ray emitting gas. As galaxy clusters form and grow throughout time by infall of galaxies and groups of galaxies, the simple picture is one of member galaxies that are transformed from blue, late-types with signs of star formation to red, early-types with no star formation. This conversion most likely happens through a combination of processes including mergers, star formation bursts, ram pressure stripping, and harassment (van Dokkum 2005; Gunn & Gott 1972; Moore et al. 1996).

This work comes at a key time in the study of star forming galaxies and AGN in high-redshift clusters. Only recently have we been able to study star formation in clusters at $z = 1$. There are only a few well-studied clusters at $z = 1$, although the number is growing rapidly and will continue to do so with upcoming Sunyaev Zel-

dovich and large sky surveys (Staniszewski et al. 2008). Additionally, traditional measures of star formation are difficult to obtain at high redshifts. $H\alpha$ shifts out of the optical band by $z \sim 0.5$. Both OII and $H\alpha$ narrow band surveys with specially designed filters (Poggianti et al. 2008; Finn et al. 2008) are possible, but optical emission line spectroscopy at high redshift is telescope time intensive, and narrow band surveys only work for the designed redshift. Both of these measures are also affected by dust obscuration. However, with *Spitzer* MIPS we are able to measure obscured star formation at large redshifts with relative ease.

That we see star formation in galaxy clusters at all is worth investigation. O & B stars live for less than 10 million years, so a single, triggered episode of star formation is likely to last for less than few tens of million years. If the infall time of a galaxy into the center of a cluster is roughly 1Gyr (assuming 1 Mpc radius and 1000km/s velocities) and all galaxies somehow have their star formation suppressed upon entering the cluster environment, we would expect to see *no* star formation in the centers of clusters, unless it is triggered, in situ, by mergers. We would therefore expect to see no blue, isolated galaxies with heightened star formation in the central regions of clusters. Furthermore, if star formation is actually first triggered and then suppressed upon cluster entry, as it has been suggested processes like ram pressure stripping could do (Bekki & Couch 2003; Kronberger et al. 2008), then we should see star formation in isolated spirals on

Electronic address: jkrick@caltech.edu

¹ Spitzer Science Center, MS 220-6, California Institute of Technology, Jet Propulsion Laboratory, Pasadena, CA 91125, USA

² Large Binocular Telescope Observatory, University of Arizona, Tucson, AZ 85721

³ Harvard-Smithsonian Center for Astrophysics, 60 Garden Street, Cambridge MA 02138

⁴ Jet Propulsion Laboratory, California Institute of Technology, Pasadena, CA, 91109

the outskirts of the clusters. Based on this timescales argument we should potentially see star formation on the edges of clusters, but not in the centers, unless it is merger driven. Star formation triggered by galaxy interactions and mergers is not dependent on cluster environment, instead on the relative velocities of the galaxies. As such this form of star formation can occur anywhere in the cluster environment or the field, and is more likely to happen in lower mass clusters or groups due to the lower relative velocities.

There is intriguing evidence that star formation rates in clusters increase with redshift out to at least $z = 0.83$ (Bai et al. 2007). We investigate if this evolution follows that in the field, implying that cluster environment does not impact star formation. We examine this claim by increasing the number of clusters studied at high redshift and extending the redshift range out to redshift one. There are only two clusters with published MIPS $24\mu\text{m}$ star formation rates at redshifts above 0.8, both at $z = 0.83$ (MS1054-03, RX J0152 Bai et al. 2007; Marcillac et al. 2007; Sain tonge et al. 2008). Koyama et al. (2008) use the Infrared Camera on Akari (Onaka et al. 2007; Murakami et al. 2007) at $15\mu\text{m}$ s to study a redshift 0.81 cluster. Although this is a mid-IR measurement of SFR, they use a different rest-frame wavelength to convert to L_{IR} which carries a different set of assumptions. Our survey is unique in that we double the number of published high redshift clusters with $24\mu\text{m}$ star formation rates by adding a large scale structure at $z = 1$ containing three clusters/groups with larger number statistics and deeper L_{IR} measurements over a large area.

In addition to star formation, we examine for the first time MIPS-detected AGN in cluster environments as a different line of evidence of galaxy activity. The same processes which affect star formation in galaxies will also effect the AGN on roughly the same timescales (Hopkins et al. 2008). AGN and star formation are linked not only because they both require a cold gas reservoir to ignite, but also due to both star formation an AGN feedback mechanisms which have the ability to destroy or remove the cold gas and halt either the star formation, the AGN activity, or both (Croton et al. 2006). AGN can put a halt to star formation by blowing out or heating the gas, and similarly star formation can use up gas thereby removing the source for a central engine. We expect the AGN fraction at high redshift to be higher than at low redshift in clusters based on evidence both in clusters and the field (Osmer 2004; Eastman et al. 2007; Kocevski et al. 2008; Galametz et al. 2009). We examine if the AGN fraction in clusters tracks the redshift evolution of that in the field or is enhanced by the cluster environment.

This paper is structured in the following manner. In §2 & §3 we discuss the data and derived photometric redshift determination. Details of the sample selection are presented in §4. In §5 we present the AGN fraction, infrared luminosities, star formation rates, colors, morphologies, and radial distributions of both the star forming and AGN samples. The paper is summarized and conclusions are drawn in §6. Throughout this paper we use $H_0 = 70\text{km/s/Mpc}$, $\Omega_M = 0.3$, $\Omega_\Lambda = 0.7$. With this cosmology, the luminosity distance at $z=1$ is 6607 Mpc, but the angular diameter distance is a factor of

$(1+z)^2$ less, or 1652 Mpc. All photometry is quoted in the AB magnitude system.

2. OBSERVATIONS & DATA REDUCTION

2.1. The IRAC Dark Field

The survey region is the IRAC Dark Field, centered at approximately 17h40m +69d. The field is located a few degrees from the north ecliptic pole (NEP) in a region which is darker than the actual pole and is in the *Spitzer* continuous viewing zone so that it can be observed any time IRAC is powered on for observing. These observing periods are called instrument “campaigns”, and occur roughly once every three to four weeks and last for about a week. Sets of long exposure frames are taken on the Dark Field at least twice during each campaign totaling roughly four hours of integration time per campaign, and these data are used to derive dark current/bias frames for each channel. The dark frames are used by the pipeline in a manner similar to “median sky” calibrations as taken in ground-based near-infrared observing to produce the Basic Calibrated Data (BCD) for all science observations. Each set of dark calibration observations collects roughly two hours of integration time at the longest exposure times in each channel.

The resulting observations are unique in several ways. The Dark Field lies near the lowest possible region of zodiacal background, the primary contributor to the infrared background at these wavelengths, and as such is in the region where the greatest sensitivity can be achieved in the least amount of time. The area was also chosen specifically to be free of bright stars and very extended galaxies, which allows clean imaging to very great depth. The observations are done at many position angles (which are a function of time of observation) leading to a more uniform final point spread function (PSF). Finally, because the calibration data are taken directly after anneals, they are more free of artifacts than ordinary guest observer (GO) observations. Over the course of the mission, the observations have filled in a region $20'$ in diameter with a total of ~ 350 hours devoted to the project; ~ 70 hours per pixel in the center of each band as of the writing of this paper. This will create the deepest mid-IR survey, exceeding the depth of the deepest planned regular *Spitzer* surveys over several times their area. Furthermore, this is the only field for which a 5+year baseline of mid-IR periodic observations is expected.

The IRAC data is complemented by imaging data in 14 other bands with facilities including Palomar, MMT, *HST*, Akari, *Spitzer* MIPS, and Chandra ACIS-I as well as Palomar optical spectroscopy. Although the entire dark field is $> 20'$ in diameter, because of spacecraft dynamics the central $\sim 15'$ is significantly deeper and freer of artifacts. Therefore, it is this area which we have matched with the additional observations. The entire dataset will be presented in detail in a future paper (Krick et al, in prep). For completeness we briefly discuss here the *Spitzer* IRAC, *Spitzer* MIPS, *HST* ACS, and Palomar optical spectroscopy as they are the most critical to this work. All space-based datasets are publicly available through their respective archives.

2.2. *Spitzer* IRAC

This work is based on a preliminary combination of 75 hours of IRAC imaging, which is $\approx 30\%$ of the expected depth not including the warm mission. The Basic Calibrated Data (BCD) product produced by the *Spitzer* Science Center was further reduced using a modified version of the pipeline developed for the SWIRE survey (Surace et al. 2005). This pipeline primarily corrects image artifacts and forces the images onto a constant background (necessitated by the continuously changing zodiacal background as seen from *Spitzer*). The data were coadded onto a regularized $0''.6$ grid using the MOPEX software developed by the *Spitzer* Science Center.

Experiments with DAOPHOT demonstrate that nearly all extragalactic sources are marginally resolved by IRAC, particularly at the shorter wavelengths, and hence point source fitting is inappropriate. Instead, photometry is done using the high spatial resolution ACS data as priors for determining the appropriate aperture shape for extracting the *Spitzer* data. We do this by first running source detection and photometric extraction on the coadded IRAC images using a matched filter algorithm with image backgrounds determined using the mesh background estimator in SExtractor (Bertin et al. 1995). This catalog is merged with the HST ACS catalog. For every object in that catalog, if the object is detected in ACS then we use the ACS shape parameters to determine the elliptical aperture size for the IRAC images. ACS shape parameters are determined by SExtractor on isophotal object profiles after deblending, such that each ACS pixel can only be assigned to one object (or the background). For objects which are not detected in ACS, but which are detected in IRAC, we simply use the original IRAC SExtractor photometry. Because of the larger IRAC beam, we impose a minimum semi-major axis radius of $2''$. In all cases aperture corrections are computed individually from PSF's provided by the SSC based on the aperture sizes and shapes used for photometry.

Final aperture photometry was performed using custom extraction software written in IDL and based on the APER and MASK_ELLIPSE routines with the shape information from SExtractor, from either ACS or IRAC as described above, using local backgrounds. Because we use local backgrounds, the measured fluxes of objects near the confusion limit should have a larger scatter than those non-confused objects, but will on average be the correct flux. This will not effect the photometric redshifts, as it will likely shift all IRAC points up or down, but not relative to each other.

Determining the detection limits of the IRAC data is complicated by varying exposure times across the field, source confusion, and our use of ACS locations as priors for photometry. Because of these three complexities, there is no one single value for the detection limit of the survey, however this work is limited by the MIPS detection limits and not IRAC or ACS. We measure nominal 95% completeness limits in the IRAC passbands from a number count diagram at 3.6, 4.5, 5.8, and $8.0\ \mu\text{m}$ to be 0.2, 0.17, 0.11, $0.11\ \mu\text{Jy}$ respectively.

2.3. *Spitzer* MIPS24

The *Spitzer* MIPS $24\ \mu\text{m}$ data were taken in large-field photometry mode with a 30-second exposure time. A 3×3 MIPS field of view grid was mapped and repeated

five times, with multiple dithers and chops totaling 224 sq. arcminutes in the center of the IRAC image. There were a total of 1080 separate exposures with a final total depth of 60 minutes per pointing on the sky. The MIPS data were processed by the *Spitzer* Science Center into individual image BCDs. However, substantial “jailbar” artifacts, as well as a significant gradient, were visible. All of the frames were forced to a common background by applying an additive constant to the entire frame. A “delta-dark” was then generated from the median of all frames; the great degree of dithering in the data allows this process to reject all actual celestial objects in the frames from the median stack. That stack was then adjusted to a median overall zero value, and then subtracted from all the data. It currently is not known whether the gradient effect is additive or multiplicative, although our experience with other Si:As arrays of this kind strongly suggests (from a physical basis) that it is additive. However, we reduced the data both ways, and found no difference at any detectable level. The data were then coadded using the MOPEX software package onto exactly the same projection system as used for IRAC, albeit with $1''.2$ pixels.

IRAF DAOFIND was used for object detection. We supply the code with the PSF FWHM and background sigma values taken by examining the image. DAOFIND then counts the flux within an annulus of diameter FWHM and flags any set of pixels as a detection where that flux is above a threshold of five sigma. To deal with confused sources, we perform object detection iteratively. After the first run through DAOFIND, all objects are subtracted from the image using a PSF determined from the detected objects. DAOFIND is then re-run on the residual image. To ensure that the iterative detection is not dominated by noise, we manually check all detections within the cluster area by eye (see §4). With the exception of a handful of galaxies, all MIPS detections appear as point sources. Photometry on all detected sources is done with the IRAF task ALLSTAR which fits PSF's to groups of objects simultaneously. An aperture correction of 1.4 is applied for flux beyond the 6.5 pixel radius at which the PSF star was normalized. This correction factor is calculated from a curve of growth based on the composite PSF star. Using this method the 3σ detection limit is $17.3\ \mu\text{Jy}$. These noise properties are comparable to the GOODS slightly longer exposure (77 minute) dataset that has a 3σ limit of $12\ \mu\text{Jy}$.

2.4. *HST* ACS

The *HST* observations consist of 50 orbits with the ACS comprising 25 separate pointings, all with the F814W filter (observed I-band). Within each pointing eight dithered images were taken for cosmic ray rejection and to cover the gap between the two ACS CCDs. The ACS pipeline CALACS was used for basic reduction of the images. Special attention was paid to bias subtraction, image registration, and mosaicing. Pipeline bias subtraction was insufficient because it does not measure the bias level individually from each of the four amplifiers used by ACS. We make this correction ourselves by subtracting the mean value of the best fit Gaussian to the background distribution in each quadrant. Due to distortions in the images, registration and mosaicing was performed with a combination of IRAF's TWEAKSHIFTS, MULTIDRIZZLE,

and SWARP v.2.16.0 from Terapix. The actual task of mosaicing the final image was complicated by the large image sizes. The single combined mosaic image is 1.7GB and reading in all 200 images (160Mb each) for combination is impossible for most software packages.

The final combined ACS image is $\sim 15'$ diameter coincident with the deepest part of the IRAC Dark Field and is made with the native $0.05''$ per pixel resolution. Photometry was performed in a standard manner with SEXTRACTOR. The 3σ detection limit for point sources is $F814W = 28.6(AB)$.

2.5. Palomar Optical Spectroscopy

The Palomar data consists of a total of four nights at the Hale 200" telescope with the COSMIC spectrograph. COSMIC, at prime focus, has a $13.6'$ field of view, and $0.4''$ pixels. Observations were made on a total of four photometric nights in June of 2007 & 2008 with the 300 l/mm grating with a dispersion of 2 \AA per pixel. We chose a slit-width of $1.5''$ to match our $1 - 1.5''$ seeing. The optical band covered by this instrument includes such spectral features as CaH&K, [OII], [OIII], H α , H β , H δ , G band, and the 4000 \AA break. During both runs we were able to observe a total of 11 slitmasks of ~ 25 galaxies each with exposure times of on average 80 minutes divided into multiple exposures. One Hg-Ar lamp and one flat was taken through each mask at the beginning of the night for calibration. Galaxies were chosen to be brighter than $r=21(AB)$ with priority given to those with MIPS 24 or $70\mu\text{m}$ detections to boost the chance of seeing an emission line and thereby getting a secure redshift.

Reduction was done with IRAF mainly through the BOGUS2006⁵ scripts. Prior to running bogus, images were overscan and bias subtracted. BOGUS itself does a 2D reduction including flat-fielding, cosmic ray removal, sky subtraction, fringe suppression and combination of frames. The same reduction is performed on both science images and arcs. The standard IRAF tasks of APALL, IDENTIFY, and DISPCOR were used to wavelength correct, trace, and extract the spectra with a secondary background subtraction for minor level changes. One dimensional spectra were extracted for a total of 200 galaxies with measurable continuum.

No single cluster galaxy was bright enough to have a spectrum observed at Palomar. Instead these spectra are used to calibrate our photometric redshifts.

3. PHOTOMETRIC REDSHIFTS

The combined IRAC and ACS catalog contains over 50,000 objects which makes acquisition of spectroscopic redshifts impractical. Even confirmation spectroscopy of red galaxies at $z = 1$ in our three candidate clusters will require many nights on 8-10m class telescopes and is therefore also impractical. In lieu of spectroscopy we use our extensive multi-wavelength, broad-band catalog to build spectral energy distributions (SEDs) using up to 13 bands (u', g', r', i', F814W, z', J, H, K, 3.6, 4.5, 5.8, $8.0\mu\text{m}$) from which we derive photometric redshifts. A full discussion of the accuracy of photometric redshift determinations is beyond the scope of this paper (but see

for example Mobasher et al. 2004; Brodwin et al. 2006; Bolzonella et al. 2000).

These SEDs are fit with template spectra derived from galaxies in the *Spitzer* wide area infrared survey survey (SWIRE; Polletta et al. 2007). These templates have been used successfully by a number of surveys at a range of redshifts for all galaxy types (Adami et al. 2008; Negrello et al. 2008; Salvato et al. 2009; Ilbert et al. 2009). Since the SWIRE templates are based on *Spitzer* observations we find them the best choice to use as models for this dataset. We use 15 templates including ellipticals, spirals, star forming galaxies, and AGN. Photometric redshifts are calculated using HYPERZ; a chi-squared minimization fitting program including a correction for interstellar reddening (Bolzonella et al. 2000; Calzetti et al. 2000).

Errors in photometric redshifts are determined by comparing the photometric redshifts with spectroscopic redshifts. Spectroscopic redshifts were determined using both IRAF tasks EMSAO and XCSAO. Specifically EMSAO searches the spectrum for both absorption and emission lines which it correlates with a given line list. XCSAO cross-correlates the spectrum with known galaxy templates which allows us to use features like the 4000 \AA break and the rest of the spectral shape to identify redshifts. Both techniques were used together to arrive at the best fit redshift for each galaxy. We used 17 spectral templates of galaxies and AGN from the compilation of the *HST* Calibration Database System (Francis et al. 1991; Kinney et al. 1996; Calzetti et al. 1994). We applied a very strict requirement that all emission and absorption features in the 1D spectra were confirmed by eye on the 2D spectra and that multiple lines be identified in all cases to avoid incorrect redshift determination due to cosmic rays or noise features from sky line subtraction.

We were able to successfully determine redshifts for 87 galaxies. This represents a conservative sample of 'good' redshift determinations defined to have either high signal-to-noise emission lines or multiple absorption lines and good cross correlations. We then compare the spectroscopic to photometric redshifts to quantify the error on the latter (Figure 1). There are cases where HYPERZ has failed to fit the correct redshift which is obvious when looking at the SED fit. Those galaxies, as characterized by a χ^2 value greater than 50, are not included in this comparison or the cluster sample below. The error on the photometric redshifts is $0.064(1+z)$. Note that this error is quoted as a function of redshift and so takes into account the increasing scatter with z . This accuracy is similar to other IRAC based multi-wavelength studies (Brodwin et al. 2006; Rowan-Robinson et al. 2008). We are confident that our quoted accuracy will hold in extrapolating our photometric redshifts out to $z=1$ because at that redshift the Balmer break is shifted into our HST ACS F814W and MMT z' which are our most sensitive bands. Secondly the peak of the stellar distribution is shifted into the IRAC bands where we have excellent coverage. It should be noted that while this level of accuracy is standard, it still implies a large volume at $z=1$ and therefore our sample selection below likely includes foreground and background interlopers. We have no leverage to remove these without exhaustive spectroscopic data.

⁵ <https://zwolfkinder.jpl.nasa.gov/stern/homepage/bogus.html>

A detailed description of the cluster properties, masses, color magnitude diagrams, and redshift distributions is given in paper one (Krick et al. 2008). Table 1 is reproduced here from that paper to summarize their properties. The first cut we make on the sample is that the objects need to have detections in at least six bands to ensure that they are real detections and not noise fluctuations. Because we use ACS locations to measure IRAC fluxes, there are cases where ACS noise (diffraction spikes, etc.) will get picked up as an object with five flux measurements. On the other hand there are real cluster galaxies which are only detected in ACS + IRAC bands because ACS is the deepest band blue-ward of IRAC and the SED's are falling sharply into the blue.

We choose twice the virial radius as the interesting physical radius that includes the dense core of the cluster but also the infall region out to roughly the turnaround radius where we might expect to find different populations of galaxies. Cluster centers are determined from the spatial distribution of the member galaxies in the F814W filter. We determine the virial radius from our X-ray detections (see Paper 1, Figure 3 for the Chandra image). The diffuse Chandra detections give us r_{500} ; the radius at which the cluster has 500 times the critical density of the Universe. From there we derive r_{vir} assuming that $r_{500} = 0.6 * r_{vir}$ (Johnston et al. 2007). This relation between r_{500} and r_{vir} comes from the average of 130,000 groups and clusters from SDSS. For our relatively low mass clusters r_{vir} is 0.7, 0.58, and 0.58 Mpc, which corresponds to 87'3, 72'8, and 72'8 respectively. Cluster two & three are too close to discuss separately as their virial radii are overlapping. We therefore consider them as one structure. The selection area will be the addition of the two circular regions. For cluster one we only consider half of the possible total area because the other half is not completely covered by our ACS imaging. While the ACS data is missing, we do have IRAC and MIPS data for this region which indicates that the cluster is symmetric and therefore we are not missing an obvious population by cutting the cluster in half.

Cluster members are chosen by their photometric redshifts. The cluster redshift distributions are centered at $z=1.0$. Our photometric errors at this redshift are 0.13, so we take as members all galaxies within $0.87 < z_{phot} < 1.13$ with HYPERZ chi-squared values less than 50. This high value cutoff of chi-squared is to keep out the catastrophic failures of HYPERZ. We do not use the red sequence to determine membership because we expect some of the member galaxies to be blue, particularly those with MIPS detections, and we don't want to bias this work against those galaxies.

Overall there are 443 member galaxies with detections in at least six bands and positions within two virial radii of any of the cluster centers, 90 of those have $24\mu\text{m}$ detections with $f_{24} > 17.3\mu\text{Jy}$. Because the PSF of MIPS is larger than the IRAC PSF, we checked by eye all MIPS matches for all objects within the area of the clusters to ensure that the correct matches with the closest centers were chosen. In the case of ambiguity, where multiple galaxies could have matched the MIPS source, those sources were not included in the analysis (approximately 10 sources). We also checked by eye those MIPS sources that were not determined to be members to make sure that a mis-match did not occur that would have kept

those objects out of the member list. This fraction of members with MIPS detections of 20% is in the right ballpark when compared to those in the literature given the varying methods of determining membership, varying depths, and different cluster masses. Bai et al. (2007) find that $13 \pm 3\%$ of cluster members are actively forming stars with $f_{24} > 50\mu\text{Jy}$.

Because we have a relatively large area at redshift one in the IRAC dark field, we are also able to make a redshift one 'field' sample of those galaxies with the exact same criteria as above (secure detections, $z=1$, and $f_{24} > 17.3$) except that they are required to be *more* distant than two virial radii of the cluster centers.

5. RESULTS & DISCUSSION

5.1. Dominant SED Shape

Because infrared flux can be generated either by dust re-radiating young star light or accretion onto a black hole, we attempt to divide the sample into sources where the MIPS flux is likely to be dominated by star formation and those where an AGN likely dominates. There is no perfect way to determine this division and it is very likely that sources have signatures of both processes (see §1). The best discriminator for the available data are the differing spectral shapes of the UV to mid-IR range for AGN and galaxies. AGN have red continua in this range owing to their rising power law shape as opposed to the falling blackbody in the same wavelength regime for galaxies. We choose to use the SED shapes as fitted by HYPERZ to determine if the source spectrum is best fit by a star forming galaxy or an AGN.

AGN candidates account for 17 of the 90 member galaxies with $24\mu\text{m}$ detections or 19% of MIPS sources and 4% of all members. These are referred to in the rest of the paper as the AGN sample. The remaining 76 galaxies have SEDs which are dominated by star formation and are referred to here as the star forming member sample. Figure 2 shows the IRAC color-color diagram for all member galaxies as a complementary method of separating AGN from star forming galaxies (Lacy et al. 2004; Stern et al. 2005). Those galaxies with MIPS $24\mu\text{m}$ detections are denoted with red (star forming galaxy) or blue (AGN) colors based on their HYPERZ fits. It is unsurprising to find that the sources tagged as AGN by their spectral fits also fit into the AGN wedge with 88% completeness but with significant contamination; 40%. The contamination is likely from intermediate redshift, PAH dominated galaxies and is similar in quantity to simulations by Sajina et al. (2005).

5.2. AGN fraction

We compare here the evolution of AGN dominated MIPS sources in clusters with that in the field. These are the first AGN fractions of MIPS-detected sources in clusters at high redshift. MIPS is sensitive to the compton thick AGN not detectable at other wavelengths. The literature does hold published X-ray-based AGN fractions in clusters. The only other IR work on this topic was published very recently by Galametz et al. (2009) based on observed frame IRAC colors and not mid-IR luminosities. Both the X-ray and near-IR studies find tantalizing evidence for an increasing AGN fraction with increasing redshift (Martini et al. 2007; Eastman et al. 2007;

Kocevski et al. 2008; Cappelluti et al. 2005). In a compilation, Eastman et al. (2007) look at the redshift evolution of the AGN fraction where AGN were selected from a sample of cluster members with $M_R < -20$. X-ray point sources with luminosities above $1 \times 10^{43} \text{ erg/s}$ were counted in comparison to the member galaxies. They find a trend of AGN fraction increasing from 0.07% to 2%, an increase of a factor of ~ 20 , over the redshift range $0.2 < z < 0.6$. Kocevski et al. (2008) look at a similar sample of X-ray sources in a supercluster at $z = 0.9$ and confirm the trend of higher AGN fraction at these higher redshifts. Although we have *Chandra* data which detect diffuse emission from two of the clusters, we are not able to do a point source analysis in the clusters to any meaningful depths.

In order to make a similar AGN fraction measurement to those described above we attempt to make similar flux cuts on our sample to find those galaxies that could potentially host AGN and the subset of those that we measure to be AGN dominated. We take the potential hosts to be all galaxies at the cluster redshift with $M_R < -20$ corresponding to $m_r < 24.8$, including K and evolution corrections for early-type galaxies. Although these sources potentially have non-early-type SED's, we chose those K and evolutionary corrections to be consistent with what was done in Eastman et al. (2007). Instead of a limit on X-ray luminosity, we use a correlation between L_x and $L_{5.8\mu\text{m}}$ (Fiore et al. 2008) to determine which of our member AGN have $L_{5.8} > 2.5 \times 10^{43} \text{ ergs/s}$. With these requirements we find there are 97 member galaxies within one virial radii of the cluster which have $m_r < 24.8$. Four of those galaxies have SED shapes of AGN and $L_{5.8} > 2.5 \times 10^{43} \text{ ergs/s}$ or 4% of the possible hosts. When compared to the Eastman et al. (2007) fraction of 0.07% at $z=0.2$, our data shows an increase of a factor of 60 of the AGN fraction in clusters from redshift 1.0 to 0.2.

We caution that this fraction depends relatively heavily on the magnitude limit of the sample and the L_x - $L_{5.8}$ correlation. If we change the magnitude cut to include fainter (brighter) galaxies down to $m_r < 25.8$ ($m_r < 23.8$) then we find a ratio of 2.5% (6.5%), both of which still represent an increase over lower redshift clusters but show a large range. If we use the Lutz et al. (2004) relation for the L_x and $L_{5.8}$ relation where the $L_x > 1 \times 10^{43} \text{ ergs/s}$ limit corresponds to $L_{5.8} > 3.5 \times 10^{43} \text{ ergs/s}$ then we find a fraction of 1%. We also caution that interpretations about the existence of a trend in AGN fraction with redshift are limited by the small number the comparison samples. At least for the radio active galaxies, Lin & Mohr (2007) find that the radio active fraction depends both on the luminosity limit of the sample and the mass of the cluster, such that more luminous galaxies and more massive clusters are likely to have higher fractions of radio active galaxies. They posit that this is really only an effect of the luminosity limit since lower mass clusters are also less likely to have high luminosity galaxies.

We now compare the evolution of AGN density (number of AGN per Mpc^3) in clusters with that in the field. Using the same cluster samples, sample selection, and caveats as above, we calculate that the AGN density in clusters evolves by a factor of ~ 500 from $z=1$ to $z=0.2$.

This number is also uncertain for the same reasons as mentioned in the previous paragraph and will drop to a factor of ~ 100 if the $L_x - L_{5.8}$ relation of (Lutz et al. 2004) is used. This measurement of density uses a volume measurement in our data which is a cylinder with depth equal to our redshift uncertainty and a radius of r_{200} . We compare this AGN density to a field sample of Ueda et al. (2003) which is a compilation of many surveys with AGN having $L_X > 1 \times 10^{43} \text{ erg/s}$. They find only a factor of ~ 10 increase in the field AGN density over the same redshift range. This implies stronger cluster evolution of the AGN density as compared to the field, or that cluster environment has influence over AGN evolution. This same trend is also reported in Eastman et al. (2007) and Galametz et al. (2009). The difference in reported strength is likely due to using different redshift ranges, AGN detection techniques, brightness cutoffs, and the other caveats mentioned above.

5.3. Star Formation Rate

Rest-frame $12\mu\text{m}$ flux correlates with total infrared luminosity (L_{IR}) which can then be converted into star formation rate (SFR). The correlation between $12\mu\text{m}$ and L_{IR} is due to the PAH emission lines. In the absence of longer wavelength data, which is not possible to get at high enough resolution and sufficient depth for these clusters, $12\mu\text{m}$ is the best wavelength from which to make the conversion; more secure than both 7 and $15\mu\text{m}$ (Chary & Elbaz 2001). The correlation between L_{IR} and SFR comes from the interstellar dust that absorbs the UV-optical light of young stars and re-radiates that energy in the infrared. With our $24\mu\text{m}$ flux and photometric redshifts we estimate the total IR luminosity using the methods of Chary & Elbaz (2001). Specifically templates from both those authors and Dale & Helou (2002) are redshifted to our source redshift and then matched to the observed $24\mu\text{m}$ flux. The best-fitting template from each model is then used to derive an average L_{IR} . From there we derive the SFR using the correlation from Kennicutt (1998). The described conversion from L_{12} to SFR is uncertain by factors of a few. However, we note that many of the conclusions of this paper rely not on the absolute SFR, but on the detection of some amount of star formation in cluster galaxies.

A histogram of L_{IR} from the star forming member sample are shown in Figure 3. 43% of the sample have infrared luminosities greater than $1 \times 10^{11} L_{\odot}$ making them luminous infrared galaxies (LIRGs). One galaxy has a flux of $1.01 \times 10^{12} L_{\odot}$ qualifying it to be an ultra-luminous infrared galaxy (ULIRG). We find a similar ratio of LIRGs to sub-LIRGs as other clusters at higher redshift. Marcillac et al. (2007) finds 60% of their star forming sample (30 galaxies) at $z = 0.83$ are LIRGs to a very similar detection limit. In a different cluster at $z = 0.83$, Bai et al. (2007) finds 41% of their sample (34 galaxies) are LIRGs. However, that survey is not as deep which means there will be more sub-LIRGs which will make this fraction lower. Geach et al. (2006) in two clusters at $z \sim 0.4$ & 05 don't go deep enough to get a good sample of sub-LIRGs.

We compare the luminosity distributions of star-forming cluster members to field MIPS-detected galaxies at redshift one. A KS test between the two distributions

shows them to have a 99% probability of being drawn from the same population. This would imply that the cluster environment does not affect the infrared luminosity of the galaxies within it. In other words, among star forming galaxies, star formation does not vary with environment.

In addition to calculating individual star formation rates per galaxy we compare the total star formation rate per cluster with other clusters at varying redshifts from the literature. The interesting physical quantity to compare is the mass-normalized SFR because SFR could vary with mass of the cluster (although see Goto 2005). We compare our redshift one clusters with 14 clusters with $0.02 < z < 0.83$ from the literature (Bai et al. 2007, and references therein). The literature sample selects only those galaxies with $\text{SFR} > 2M_{\odot}/\text{yr}$ within $0.5r_{200}$. Our SFR cutoff is similar ($3M_{\odot}/\text{yr}$) and we truncate our sample to match the $0.5r_{200}$ radius.

In Figure 4 the literature clusters are shown with triangles and the composite of our redshift one clusters with an asterisk. Error bars in all cases are 1σ errors taken from the combination of both mass and SFR errors. Our three clusters are relatively low mass clusters, and because there is some concern about a relation between mass-normalized SFR and mass, we also denote the other lower mass clusters ($M < 5 \times 10^{14}M_{\odot}$) in this figure with squares. These lower mass clusters in the comparison sample are still of higher mass than our redshift one clusters. However, hierarchical formation tells us that redshift one clusters will grow in mass by the time they reach redshift zero. Comparing clusters of the same mass across a large redshift range would then also introduce a bias into the sample. Our three redshift one clusters are suggestive of continuing the trend of higher redshift clusters having a larger amount of mass-normalized SFR. This is true both when looking at the whole sample of lower redshift clusters and also confining the sample to the five lowest mass, lower redshift clusters. It will be important to compare our clusters to even lower mass, low-redshift counterparts when that data becomes available.

SFR can also be computed from different wave-bands. A detailed discussion of the varying methods and their relative strengths and weaknesses is beyond the scope of this paper, but see Kennicutt (1998) and references thereto for such a discussion. We would like to compare our results on the redshift evolution of the mass-normalized SFR with other measures from the literature, however such measures are not published covering the entire redshift range presented here. $H\alpha$ and OII derived SFR for clusters at $z < 0.8$ are presented in Finn et al. (2008) and Poggianti et al. (2008) and those are in agreement with the mid-IR determined values (Bai et al. 2007).

The comparison with the field SFR evolution is also interesting. We know that the SFR density (SFRD) in the universe peaks around $1 < z < 2$ and then declines to today (Madau et al. 1998; Lilly et al. 1996). A recent compilation of SFRD measurements, Hopkins & Beacom (2006) show a factor of $5 \sim 10$ drop in the SFRD from redshift 1.0 to 0.1 in the field. We calculate the SFRD of our clusters at $z=1$ and compare this to the SFRDs for the four lowest redshift clusters in the literature sample with an average redshift of $z=0.1$. We do this using the

sample confined to $0.5r_{200}$ for ease of comparison. We find a drop in SFRD from $z=1.0$ to $z=0.1$ of a factor of 40. This could imply that while the distribution of IR luminosities of $z=1$ cluster galaxies are similar to the field, the suppression of star formation happens more quickly in clusters than in the field, implying that the cluster environment is more efficient in the suppression of star formation and AGN than the field. Our data suggest this is the case, but a larger, more uniform sample is required for confirmation.

5.4. Color

We explore the colors of the MIPS-detected, star forming sources in the clusters for the purpose of understanding if the red galaxies in the clusters are red because they have no star formation, or if they are red due to dust. Figure 5 shows the distribution of rest-frame B-K colors of the MIPS-detected, star forming member galaxies (dashed line) and all cluster members (solid line). We use the dotted line as the dividing line between the blue cloud and the red sequence (see Paper 1).

We correct galaxy colors for dust reddening using the extinction as measured by the HYPERZ SED fits and the Calzetti et al. (2000) extinction law. Another possible way to make this correction is with Balmer line spectroscopy. However, with a sample of greater than 2000 galaxies at $0.05 < z < 1.5$, Cowie & Barger (2008) find that SED fitting is a comparable technique and in fact use the SED fitted extinction instead of the Balmer ratios even when they do have spectroscopy. The corrected colors for our sample are shown on the right side of Figure 5.

There is a significant amount of extinction at these wavelengths, particularly at rest-frame B where extinctions range from $A_B = 0 - 1.6$, showing that many of these galaxies are dust reddened star forming sources and in large part not galaxies that are red due to age. The corrected histogram shows a very different distribution, with 57% of the MIPS sources moving from the red sequence to the blue cloud. This is consistent with Cowie & Barger (2008) who find roughly half of their MIPS-detected red sequence galaxies move off of the red sequence after correction. These data tell us that the MIPS sources do not form a uniquely colored population and are instead very dusty galaxies.

5.5. Morphology

We examine morphologies of the MIPS sample both with SED fitting and a by-eye determination for the purpose of determining which types of galaxies are mid-IR bright in clusters at $z = 1$. One method of determining galaxy type is by fitting templates to its SED. This really is a measure of the SED shape used as a proxy for morphology. The strength of this method is that it allows us to easily compare field to cluster galaxies using the same objective criteria. SED shape has already been determined for all galaxies with HYPERZ while fitting for photometric redshifts. In Figure 6 we show the histogram of types of galaxies from this analysis arranged from star forming galaxies to AGN. The solid line shows the member galaxies with $24\mu\text{m}$ detections and the dashed histogram is the normalized histogram of all $24\mu\text{m}$ detections across the entire field. As expected there are rela-

tively few early-type galaxies, and a relatively large number of late-types and AGN. There are very similar distributions from cluster to field. This is perhaps hinting that cluster environment is not effecting the morphologies of the mid-IR bright galaxies, much like the infrared luminosities of star forming galaxies being unaffected by environment in §5.3.

Since there are only 90 galaxies with MIPS detections at the cluster redshift, we classify their morphologies manually by eye. For this, we use the data with the best resolution which is the *HST* ACS F814W data, corresponding to rest-frame B-band, with $0.5''/\text{pixel}$ resolution. Training for this was done with examples from the online SDSS GalaxyZoo⁶ which has color images at a range of redshifts. We choose a very simple classification scheme meant to divide those galaxies with visible signs of interactions from those without. To this end we choose five categories which fit all galaxies with the exception of seven galaxies because they were either not imaged with ACS or are too near a bright star or it's diffraction spikes to clearly classify. The five categories are Compact, Elliptical, Spiral, Irregular/disk, and Irregular/merger. We stick to very basic definitions to avoid ambiguous classifications. Things fall into the compact, elliptical, or spiral classes if they have classical forms of those shapes. Although compact classified objects have the shape of a PSF, they have been confirmed to be non-stellar based on their SED fits. Spirals include anything with a disk that doesn't look disturbed or asymmetric in any way. Irregular galaxies are anything that does not fit one of the classical descriptions. Because the Irregular galaxies make up such a large fraction of the sample, we have sub-divided that classification into those systems that clearly have multiple nuclei or obvious tidal tails (Irregular/merger) and all other irregular galaxies, mainly disturbed disks (Irregular/disk). This differentiation of the irregular galaxies may indicate something about the timescales of interaction histories with the Irregular/merger classification going to those objects at earlier stages of interaction, and Irregular/disk going to those objects at later stages. Figure 7 shows examples from our sample of our morphological classification.

Table 2 shows the morphological distribution for the entire sample as well as subsamples based on color and infrared luminosity (§5.4 & 5.3). Of the entire sample of member galaxies with MIPS detections, the majority of them are either spirals or irregulars (81%), unsurprisingly. Specifically, 25% of the sources show obvious signs of interactions or mergers. There are potentially more interacting galaxies whose tidal features are too low in surface brightness for us to detect but this cannot account for all of them. In the cases of the galaxies which show signs of interaction we do not need to invoke a cluster environment driven process to trigger star formation, we can assume here that the merger has triggered star formation. The remainder (75%) of the sources which do not show signs of interaction must have had their SF triggered by some physical process that can occur within the cluster environment such as ram pressure stripping or harassment (Gunn & Gott 1972; Moore et al. 1996). In the next section we discuss the location of this SF to determine if it is on the cluster outskirts and therefore is

potentially residual SF after suppression upon entering the cluster environment, or if it is truly being triggered by some cluster process ongoing inside the cluster and suppression is not complete at the cluster edges.

The majority of compact sources are part of the AGN sample based on SED fitting. Other compact determined galaxies are likely ellipticals where the lower surface brightness outer parts of the bulge are not visible at $z \sim 1$.

The ellipticals are an interesting population in which to find star formation. From our original sample selection of 443 member galaxies, less than two percent are ellipticals with MIPS detections. About half of the elliptical galaxies have red colors both before and after extinction correction implying that there are a few legitimate red ellipticals with star formation signatures. Some of these are possibly mis-classifications because of projections or surface brightness dimming of a disk component or AGN mis-classifications. Most of these ellipticals are sub-LIRGs so they do not have the higher SFRs in the sample. It is possible that we are seeing residual star formation after a merger, but it is hard to imagine that the morphological change would precede the end of the triggered star formation. The last possibility is that we see signs of dusty star formation in elliptical galaxies that goes against traditional findings that elliptical galaxies have no star formation, at least not at the SFRs to which we are sensitive ($> 3M_{\odot}$). Optically red, morphologically elliptical galaxies with excess $24\mu\text{m}$ emission have also been found in SWIRE, GOODS, and the Bootes fields (Rodighiero et al. 2007; Davoodi et al. 2006; Brand et al. 2009). While some of these show AGN signatures, some are attributed to star formation.

When we split the sample based on infrared luminosity we see that the spirals and irregulars make up the majority of the LIRGs (90%) but a lesser percentage of the sub-LIRGs (73%) due to the higher fraction of compact and elliptical sources. Also interesting is that the irregular population is split evenly between LIRGs and sub-LIRGs, and 60% of the spirals are LIRGs. In summary, LIRGs in clusters are most likely to be blue spirals or irregulars. Dividing by morphology, spirals are more likely to be LIRGs, irregulars are equally likely to be LIRGs or sub-LIRGs, and ellipticals are most likely sub-LIRGs.

Our findings of the ratios of morphological types in clusters is similar to other published cluster values at high redshifts. In their survey of a redshift 0.83 cluster, Bai et al. (2007) find that of their IR-detected galaxies, 20%, 63%, and 16% of them are early-type, late-type, and irregular galaxies, respectively, and 32% show signs of mergers/interactions. Also for a redshift 0.83 cluster, Marcillac et al. (2007) find 75% spirals (including S0s, since we would have given those a spiral designation) and 25% irregulars. Again these are only rough comparisons with the caveat that all of these studies have only small samples which vary in cluster mass, density, and dynamical state, etc., all things which might have an effect on the morphologies and infrared luminosities of member galaxies.

5.6. *Distribution of Star Forming Galaxies*

We examine the location of the MIPS sources in the clusters with the goal of measuring if they are more or less concentrated than the non-MIPS sources which

⁶ <http://www.galaxyzoo.org/>

would imply that they preferentially live in the centers or outskirts of the clusters. We make this comparison using cumulative distributions and a KS test which is the most straightforward way to determine if two continuous, unbinned, distributions are drawn from the same parent distribution. This is the best statistical test to make this measurement given a relatively small sample of galaxies especially when we split the sample by galaxy property to examine the trends below. KS tests are relevant on samples sizes larger than ~ 5 (Press et al. 2007). Figure 8 shows unbinned cumulative distributions as a function of distance from the cluster center. All three clusters are combined here on the top left panel and distance from center is taken to be distance to the nearest cluster center. In the top left panel we show the distribution of the MIPS-detected star forming galaxies (solid) and AGN(dashed) compared to both all cluster members (dotted) and the field(dot-dashed). We check that increasing the sample to include objects with 'only' five flux detections does not change the shape of the cumulative distribution (see §4 for a discussion of the number of detections required for an object to be included in the sample).

The first thing to notice is that all of the cluster samples (those with and without MIPS detections) show evidence of being significantly more centrally concentrated than a comparison field sample as measured in circles of the same area in the field. A KS test on the composite sample shows less than 1E-7% chance that they are drawn from the same parent population. This is both nice confirmation of our photometric redshifts and proof that star formation occurs in cluster environments. In a similar experiment we determine the space density of MIPS sources in the composite tri-cluster area compared to similar area in the field. In field regions of the same area as the cluster, we measure the mean space density to be 43 ± 15 sources whereas we detect 90 sources in the cluster area which is a greater than 3σ overdensity. The cluster environment has clearly enhanced the number of mid-IR sources among its member galaxies. This is usually, but not always the case in the literature. Geach et al. (2006) find only a very minimal overdensity in MS0451-03 at $z=0.55$. Marcillac et al. (2007); Bai et al. (2007); Gallazzi et al. (2008) all find significant overdensities when compared to the field.

Secondly, the top left panel of figure 8 shows that the star forming MIPS members and the non-MIPS-detected members are consistent with having the same spatial distribution. A KS test shows they have a 97% chance of being drawn from the same population. We investigate this trend further by dividing our cluster sample. The top right and bottom panels of figure 8 show the cumulative distributions for the separated clusters. Interestingly, cluster 1 on it's own has a significantly different spatial distribution which has only a 1% probability of being drawn from the same population as the rest of the member galaxies. In this cluster we see a less concentrated distribution of star forming galaxies until roughly 1 virial radius (0.7 Mpc) at which point the distribution steeply rises, indicating a possible excess of star forming galaxies just beyond that radius.

The other two clusters show no such trend. One possible explanation is that there is some critical cluster property different between these two sets driving the differ-

ence in spatial distributions. One could imagine that cluster property to be mass or evolutionary state. Cluster one is both more massive than the other clusters and is more relaxed in the sense that it appears to have already formed a cD galaxy whereas the other clusters are in the process of forming their cD's (see figure 7 for an image of the central galaxy in cluster 2). A larger sample is required to examine these differences. A second possibility is that these two clusters represent a complex structure in our 2D image. They are relatively close to each other (overlapping virial radii at the same photometric redshifts) that it is possible these two clusters actually reside in the same potential well, or that one is falling in towards the center of the other, which would make our choice of centers meaningless. Because of their nearness, we could imagine that projection effects could dilute any potential signal of a less concentrated distribution.

We have found that different clusters potentially exhibit different spatial distributions in their star forming galaxies, which is also found in Geach et al. (2006). Coia et al. (2005); Bai et al. (2007); Marcillac et al. (2007); Gallazzi et al. (2008); Fadda et al. (2008) and Koyama et al. (2008) report the detection of an intermediate density at which cluster star forming galaxies congregate, but this is also not found in the work of Biviano et al. (2004). The comparison of literature samples is not straightforward because of the differing cluster properties (mass, virialization, and structure) and differing sampling methods including flux detection levels and accounting for AGN contamination. Also in some cases the evidence for star forming galaxies to preferentially lie at intermediate densities is not statistically strong ($< 3\sigma$). For these listed reasons, and that different authors use different measures of local environment, it is not practical to compare literature samples.

We further discuss the cumulative distributions of the sample with a focus on infrared luminosity, morphology, and color. We continue to discuss the sample as the combination of all three clusters which does not effect the remainder of the results.

5.6.1. Distribution by L_{IR}

We divide the sample of star forming galaxies based on infrared luminosity in the top right panel of Figure 9. Those with LIRG luminosities or above are shown with the solid line, and those with sub-LIRG luminosities are shown with the dotted line. The LIRGs do appear to be more centrally concentrated than the sub-LIRGS, however a KS test is inconclusive giving a 53% probability that they are drawn from the same population. This inconclusiveness means that we cannot rule out the possibility that sub-LIRGs have a different, less concentrated, distribution than LIRGs. This leaves open the possibility that at lower redshift where surveys are likely to be deeper than high redshift surveys, the lower luminosity sub-LIRGS might dominate the population thereby giving the appearance of being overall less concentrated than the other member galaxies. This could be a reason why lower redshift surveys find less concentrated spatial distributions, but does not explain the preferred density peaks reported in those studies.

5.6.2. Distribution by Morphologies

We now investigate the location of the star forming galaxies by splitting the sample on morphology. If the spirals are less centrally concentrated it could suggest that the cluster environment is able to burst and then suppress star formation in normal non-interacting galaxies. The remaining star formation activity that we see closer to the center is then the result of galaxy interactions. The top right panel of Figure 9 shows the cumulative distribution of the spiral sample (solid line) and the likely merger sample (dotted line), based on the morphologies as determined by eye in §5.5. There is again tantalizing but inconclusive evidence that the spirals are less centrally concentrated. A KS test on these two samples gives a 65% chance that the two populations draw from the same parent distribution which prevents us from concluding either that there are or not more centrally concentrated. We also plot the distribution of the elliptical star forming galaxies but small sample size (7 galaxies) prevents us from making conclusions. Projection effects also complicate this analysis since we do not know the 3D location of the member galaxies.

The inconclusive tests for both morphology and L_{IR} radial distributions are probably telling us that there is another variable which is confusing these tests. A larger sample size of clusters split by cluster properties is desirable to further test our hypotheses in these cases.

5.6.3. Distribution by Color

To understand more about spatial distribution of the MIPS sources we further divide the sample of star forming galaxies by color into a red and blue sample based on their uncorrected magnitudes. The dividing line is taken to be the blue edge of the red cluster sequence as described in paper one and shown in Figure 5. The same division is made for the non-MIPS-detected cluster members and the results are shown in the bottom left panel of Figure 9. The left, more centrally concentrated fork of the distribution shows the red galaxies while the right fork shows the distribution of the blue galaxies with solid lines for the MIPS members and dotted lines for the non-MIPS member galaxies. Again we see that the MIPS members and non-MIPS members show similar distributions (KS = 76% for red and 70% for blue) while we see a clear difference between red and blue galaxies (KS < 0.01%) with blue avoiding the central dense regions of the clusters. This is a classic finding that blue galaxies generally don't inhabit dense environments (Butcher & Oemler 1984; Pimbblet 2003).

However, if we look at the distribution of the reddening corrected colors (§5.4) we find a different story; bottom right panel of Figure 9. Here we see that the blue non-MIPS -detected members still show the same trend of the blue galaxies avoiding the centers. In contrast to the non-reddening corrected color distributions, all the MIPS-detected galaxies now have the same distribution regardless of color (KS = 94%). In other words, the formerly red galaxies are co-spatial with the blue galaxies. This is just showing us again that many of the observed red galaxies are actually dusty blue galaxies and are not red because they are old.

5.7. Distribution of AGN

We examine the distribution of cluster AGN compared to the MIPS -detected star forming galaxies. Figure 8

includes the cumulative distribution of MIPS -detected AGN cluster members as the dashed lines. A KS test between the AGN and star forming members in the combined distribution is inconclusive, showing a 50% probability of drawing from the same population. A KS test on clusters two and three shows a 90% probability of deriving from the same population. It is interesting that the AGN and star forming galaxies appear to have similar distributions in two of the clusters. The similar distribution could imply that the same physical mechanism triggers AGN and star formation. In a similar case to the SF galaxies, because cluster one shows a different AGN distribution from the other clusters, we are unable to ferret out the underlying causes of the distributions. The literature is similarly inconclusive. A radio sample from Lin & Mohr (2007) shows that AGN are more concentrated than cluster galaxies with the radio-brightest being the most concentrated. A sample of eight low-intermediate redshift clusters with X-ray-detected AGN reveal the same trend (Martini et al. 2007). However, in a supercluster at $z=0.9$, Kocevski et al. (2008) find that X-ray AGN are more likely located in the intermediate regions, avoiding the densest cluster centers. The differences in samples between Radio, X-ray, and Mid-IR selections and differences between depths and cluster characteristics may be the source of these differences. A larger sample is necessary to make progress on this topic.

6. CONCLUSION

We have used a multi-wavelength dataset based on extremely deep *Spitzer* IRAC data to examine the nature of mid-IR sources in a large scale structure of three clusters at redshift one. There are 90 members of the clusters with MIPS detections within two virial radii of the cluster centers, of which 17 appear to have SEDs dominated by AGN and the rest dominated by star formation. With the samples of AGN and star forming sources we examine the total infrared luminosities, star formation rates of individual galaxies and of the structure as a whole, colors, morphologies, and distributions whereby we come to the conclusions listed below.

- We look for evolution in the AGN fraction with redshift. In a comparison with X-ray surveys we find a continued increase in the AGN fraction out to redshift one with trepidation over the accuracy of the conversion between $L_{5.8}$ and L_X . In addition the magnitude of the increase in AGN fraction is higher in clusters than in the field. If an effect of AGN activity is to suppress star formation through a feedback mechanism, then the measured large number of AGN at higher redshifts indicates that there will be many galaxies for which AGN feedback may be a significant player in turning off star formation in lower redshift clusters. Secondly because of the more rapid decrease in AGN fraction in clusters compared to the field, we conclude that cluster environment has an effect on the decline of the AGN population.
- For the sample of star forming members, we use the $24\mu\text{m}$ flux (rest frame $12\mu\text{m}$) to estimate total infrared luminosity. The distribution of infrared luminosities shows that about half of the sample have

infrared luminosities consistent with being LIRGs while the other half are sub-LIRGs. That distribution is consistent with the field at redshift one, as measured from other regions in our data, implying that the cluster environment does not have an effect on the infrared luminosities of the galaxies within it.

- Total infrared luminosity is converted to star formation rate. As a whole, the summed, mass-normalized cluster star formation rate is higher at $z = 1$ than in counterparts at lower redshift. The measured decrease of SFRD from $z=1$ to 0 is larger than the decrease measured in the field implying that suppression of star formation is accelerated in the cluster environment.
- Based on SED fitted extinction values at rest frame B-band, we find that MIPS sources in clusters are mainly highly extinguished, dusty, intrinsically blue galaxies. A few are intrinsically old red galaxies.
- Morphologies of the MIPS-detected sources are determined by eye from the *HST* rest-frame B-band images. The majority of sources (81%) are spirals or irregulars. There are a few elliptical galaxies (8%), the majority of which have sub-LIRG luminosities. Potentially some of these are misclassifications, but some are real detections of dusty star formation of greater than three solar masses per year in an elliptical galaxy. The LIRGs in clusters are most likely to be blue spirals or irregulars. A large fraction (at least 25%) show obvious signs of interactions. This implies that some cluster galaxies have SF triggered by the cluster environment and not solely by merger processes which are not cluster environment dependent.
- Cluster MIPS sources are significantly more concentrated than a field sample at redshift one showing that they are indeed members of the cluster. Cluster characteristics appear to influence the spatial distribution of the star forming member galaxies. One of our clusters shows the MIPS sources with a less concentrated distribution than the other members. However, the other two clusters have MIPS sources with the same distribution as the member galaxies implying that complete suppression has not occurred due to the cluster environment. There is inconclusive evidence for LIRGs and irregular galaxies separately to be more centrally concentrated than sub-LIRGs and spirals respectively. When using uncorrected magnitudes, galaxies blue-ward of the red sequence are significantly less concentrated than red galaxies. However when using reddening corrected galaxy colors, we find all MIPS-detected cluster members to have the same distribution confirming that the MIPS

sources really are dusty, star forming, blue galaxies and not a separate population.

Cluster environment does seem to have an effect on the evolution of AGN fraction and SFR from redshift one to the present, but amongst the IR active galaxy sample, environment does not affect the infrared luminosities. This may be saying that whatever triggers the star formation in clusters has the same effect on the galaxies in the clusters as whatever triggers star formation in the field, eg. star formation looks the same regardless of environment. Or, in other words, the effect of star formation on a galaxies infrared luminosity is independent of triggering mechanism. But, the cluster environment does encourage SFR and AGN fraction to decline more rapidly with time over the field implying that the cluster environment does have an effect on a galaxies activeness, either SF or AGN. While some of our galaxies show signs of interaction as the likely triggering mechanism, it seems likely that other cluster environment driven effects are also able to trigger SF within the cluster. This is based both on morphological indicators of SF and the distributions of SF galaxies. In two clusters we see no evidence for a suppression of star formation in the inner regions of the clusters as we would expect if there were a density cutoff for triggering SF. As always, a larger sample of clusters with deeper mid-IR measurements is desirable.

This research has made use of data from the Two Micron All Sky Survey, which is a joint project of the University of Massachusetts and the Infrared Processing and Analysis Center/California Institute of Technology, funded by the National Aeronautics and Space Administration and the National Science Foundation. This work was based on observations obtained with the Hale Telescope, Palomar Observatory as part of a continuing collaboration between the California Institute of Technology, NASA/JPL, and Cornell University, the *Spitzer* Space Telescope, which is operated by the Jet Propulsion Laboratory, California Institute of Technology under a contract with NASA, the MMT Observatory, a joint facility of the Smithsonian Institution and the University of Arizona, and the NASA/ESA Hubble Space Telescope, obtained at the Space Telescope Science Institute, which is operated by the Association of Universities for Research in Astronomy, Inc., under NASA contract NAS 5-26555. These observations are associated with program #10521. Support for program #10521 was provided by NASA through a grant from the Space Telescope Science Institute, which is operated by the Association of Universities for Research in Astronomy, Inc., under NASA contract NAS 5-26555.

Facilities: Hale (LFC, WIRC, COSMIC), MMT (Megacam), HST (ACS), Spitzer (IRAC, MIPS), Akari, CXO (ACIS)

REFERENCES

- Adami, C., Ilbert, O., Pelló, R., Cuillandre, J. C., Durret, F., Mazure, A., Picat, J. P., & Ulmer, M. P. 2008, *A&A*, 491, 681
 Bai, L. et al. 2007, *ApJ*, 664, 181
 Bekki, K., & Couch, W. J. 2003, *ApJ*, 596, L13
 Biviano, A. et al. 2004, *A&A*, 425, 33
 Bolzonella, M., Miralles, J.-M., & Pelló, R. 2000, *A&A*, 363, 476
 Brand, K. et al. 2009, *ApJ*, 693, 340
 Brodwin, M. et al. 2006, *ApJ*, 651, 791
 Butcher, H., & Oemler, A. 1984, *ApJ*, 285, 426

- Calzetti, D., Armus, L., Bohlin, R. C., Kinney, A. L., Koornneef, J., & Storchi-Bergmann, T. 2000, *ApJ*, 533, 682
- Calzetti, D., Kinney, A. L., & Storchi-Bergmann, T. 1994, *ApJ*, 429, 582
- Cappelluti, N., Cappi, M., Dadina, M., Malaguti, G., Branchesi, M., D'Elia, V., & Palumbo, G. G. C. 2005, *A&A*, 430, 39
- Chary, R., & Elbaz, D. 2001, *ApJ*, 556, 562
- Coia, D. et al. 2005, *A&A*, 431, 433
- Cowie, L. L., & Barger, A. J. 2008, *ApJ*, 686, 72
- Croton, D. J. et al. 2006, *MNRAS*, 365, 11
- Dale, D. A., & Helou, G. 2002, *ApJ*, 576, 159
- Davoodi, P. et al. 2006, *MNRAS*, 371, 1113
- Eastman, J., Martini, P., Sivakoff, G., Kelson, D. D., Mulchaey, J. S., & Tran, K.-V. 2007, *ApJ*, 664, L9
- Fadda, D., Biviano, A., Marleau, F. R., Storrie-Lombardi, L. J., & Durret, F. 2008, *ApJ*, 672, L9
- Finn, R. A., Balogh, M. L., Zaritsky, D., Miller, C. J., & Nichol, R. C. 2008, *ApJ*, 679, 279
- Fiore, F. et al. 2008, *ArXiv e-prints*
- Francis, P. J., Hewett, P. C., Foltz, C. B., Chaffee, F. H., Weymann, R. J., & Morris, S. L. 1991, *ApJ*, 373, 465
- Galametz, A. et al. 2009, *ArXiv e-prints*
- Gallazzi, A. et al. 2008, *ArXiv e-prints*
- Geach, J. E. et al. 2006, *ApJ*, 649, 661
- Goto, T. 2005, *MNRAS*, 356, L6
- Gunn, J. E., & Gott, J. R. I. 1972, *ApJ*, 176, 1
- Hopkins, A. M., & Beacom, J. F. 2006, *ApJ*, 651, 142
- Hopkins, P. F., Hernquist, L., Cox, T. J., & Kereš, D. 2008, *ApJS*, 175, 356
- Ilbert, O. et al. 2009, *ApJ*, 690, 1236
- Johnston, D. E. et al. 2007, *ArXiv e-prints*, 709
- Kennicutt, Jr., R. C. 1998, *ARA&A*, 36, 189
- Kinney, A. L., Calzetti, D., Bohlin, R. C., McQuade, K., Storchi-Bergmann, T., & Schmitt, H. R. 1996, *ApJ*, 467, 38
- Kocevski, D. D., Lubin, L. M., Lemaux, B. C., Gal, R., Fassnacht, C. D., Lin, R., & Squires, G. K. 2008, *ArXiv e-prints*
- Koyama, Y. et al. 2008, *MNRAS*, 1302
- Krick, J. E., Surace, J. A., Thompson, D., Ashby, M. L. N., Hora, J. L., Gorjian, V., & Yan, L. 2008, *ArXiv e-prints*
- Kronberger, T., Kapferer, W., Ferrari, C., Unterguggenberger, S., & Schindler, S. 2008, *A&A*, 481, 337
- Lacy, M. et al. 2004, *ApJS*, 154, 166
- Lilly, S. J., Le Fevre, O., Hammer, F., & Crampton, D. 1996, *ApJ*, 460, L1+
- Lin, Y.-T., & Mohr, J. J. 2007, *ApJS*, 170, 71
- Lutz, D., Maiolino, R., Spoon, H. W. W., & Moorwood, A. F. M. 2004, *A&A*, 418, 465
- Madau, P., Pozzetti, L., & Dickinson, M. 1998, *ApJ*, 498, 106
- Marcillac, D., Rigby, J. R., Rieke, G. H., & Kelly, D. M. 2007, *ApJ*, 654, 825
- Martini, P., Mulchaey, J. S., & Kelson, D. D. 2007, *ApJ*, 664, 761
- Mobasher, B. et al. 2004, *ApJ*, 600, L167
- Moore, B., Katz, N., Lake, G., Dressler, A., & Oemler, A. 1996, *Nature*, 379, 613
- Murakami, H. et al. 2007, *PASJ*, 59, 369
- Negrello, M. et al. 2008, *ArXiv e-prints*
- Onaka, T. et al. 2007, *PASJ*, 59, 401
- Osmer, P. S. 2004, in *Coevolution of Black Holes and Galaxies*, ed. L. C. Ho, 324+
- Pimblett, K. A. 2003, *Publications of the Astronomical Society of Australia*, 20, 294
- Poggianti, B. M. et al. 2008, *ApJ*, 684, 888
- Polletta, M. et al. 2007, *ApJ*, 663, 81
- Press, W., Teukolsky, S., Vetterling, W., & Flannery, B. 2007, *Numerical Recipes 3rd Edition: The Art of Scientific Computing* (Cambridge University Press)
- Rodighiero, G. et al. 2007, *MNRAS*, 376, 416
- Rowan-Robinson, M. et al. 2008, *MNRAS*, 386, 697
- Saintonge, A., Tran, K.-V. H., & Holden, B. P. 2008, *ApJ*, 685, L113
- Sajina, A., Lacy, M., & Scott, D. 2005, *ApJ*, 621, 256
- Salvato, M. et al. 2009, *ApJ*, 690, 1250
- Staniszewski, Z. et al. 2008, *ArXiv e-prints*
- Stern, D. et al. 2005, *ApJ*, 631, 163
- Surace, J. A., Shupe, D. L., Fang, F., Evans, T., Alexov, A., Frayer, D., Lonsdale, C. J., & SWIRE Team. 2005, in *Bulletin of the American Astronomical Society*, Vol. 37, *Bulletin of the American Astronomical Society*, 1246+
- Ueda, Y., Akiyama, M., Ohta, K., & Miyaji, T. 2003, *ApJ*, 598, 886
- van Dokkum, P. G. 2005, *AJ*, 130, 2647

TABLE 1
CLUSTER CHARACTERISTICS

Cluster	ra J2000 (deg)	dec J2000 (deg)	N_{gals} $r < 500Kpc$	z_{peak}^a	L_x (0.5-2.0 Kev) $1 \times 10^{43} \text{erg/s}$	M_{500} $1 \times 10^{13} M_{\odot}$
1	264.68160	69.04481	215	1.0 ± 0.1	3.6 ± 0.6	6.2 ± 1.4
2	264.89228	69.06851	255	1.0 ± 0.1	1.6 ± 0.7	3.6 ± 1.4
3	264.83102	69.09031	241	1.0 ± 0.2	$\leq 1.6 \pm 0.7$	$\leq 3.6 \pm 1.1$

^a Redshift peak and one sigma uncertainty are measured from a Gaussian fit to the redshift distribution.

TABLE 2
MORPHOLOGIES OF MIPS24 MEMBERS

Galaxy Morphology	All	LIRGs	sub-LIRGs
Compact	9 (11%)	2 (5%)	7 (16%)
Elliptical	7 (8%)	2 (5%)	5 (11%)
Spiral	30 (35%)	18 (44%)	12 (27%)
Irr/Disk	18 (21%)	9 (22%)	9 (21%)
Irr/Merger	21 (25%)	10 (24%)	11 (25%)
Total	85 (100%)	41 (100%)	44 (100%)

NOTE. — The first data column shows the morphology breakdown for all member galaxies with MIPS detections. Columns 2 & 3 divide all members into those with LIRG and sub-LIRG luminosities. Percentages are of the galaxies only within the column shown.

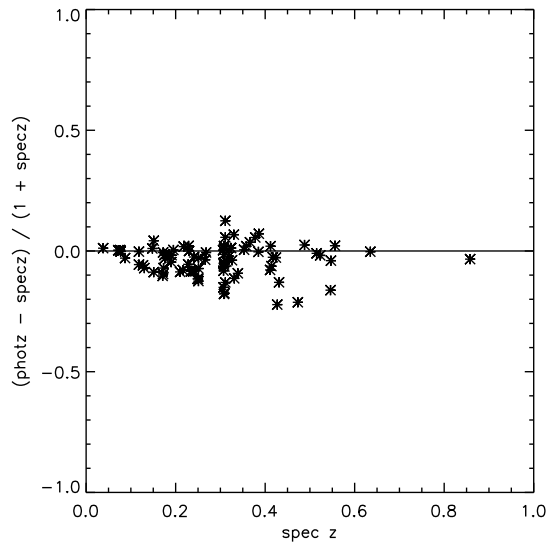


FIG. 1.— Comparison of spectroscopically and photometrically determined redshifts. The scatter implies an error on the photometric redshifts of $0.064(1+z)$.

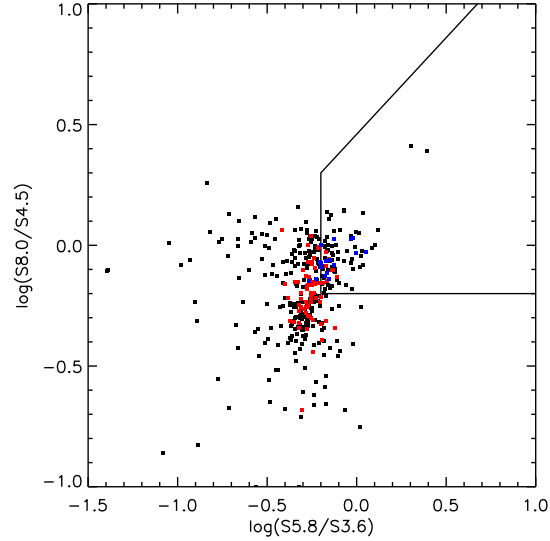


FIG. 2.— IRAC color color diagram after Lacy et al. (2004). All cluster member galaxies are shown in black. Those with $24\mu\text{m}$ detections are color coded red for star forming and blue for AGN based on HYPERZ fits of their SEDs. Lines show the expected location of AGN based on having red colors in both axes. The member galaxies on the color color diagram are where we expect redshift one galaxies to be (Sajina et al. 2005) based on position of PAH features and the stellar peak, which is a nice confirmation of our photometric redshifts.

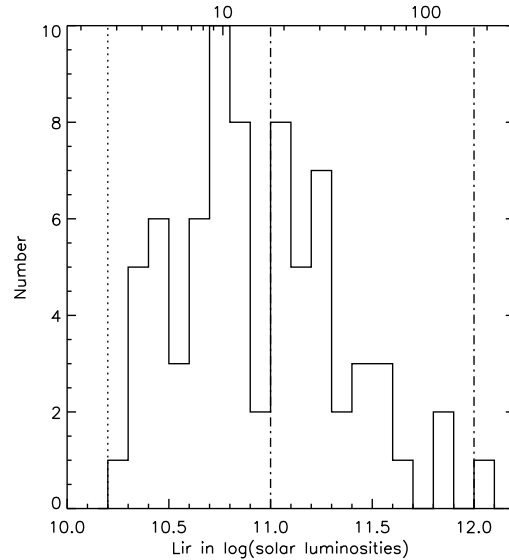


FIG. 3.— Histogram of infrared luminosity of the star forming member galaxies. The top axis shows SFR in M_{\odot}/year . Dot-dashed lines show the cutoff for LIRGs and ULIRGs at 1×10^{11} and 1×10^{12} L_{\odot} respectively. 43% of the sample are above the LIRG cutoff. The dotted line shows the completeness limit of the MIPS data.

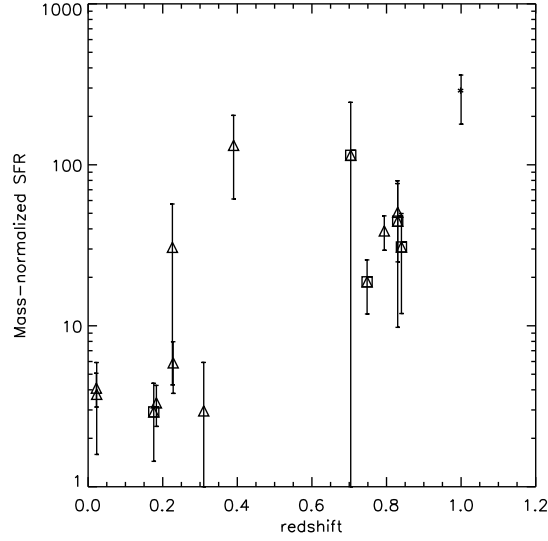


FIG. 4.— Mass normalized star formation rate as a function of redshift. The asterisk represents the three redshift one clusters from this survey. The triangles are from the literature. Those literature clusters with masses less than 5×10^{14} have their triangles surrounded by squares. Error bars come from a combination of mass and SFR errors.

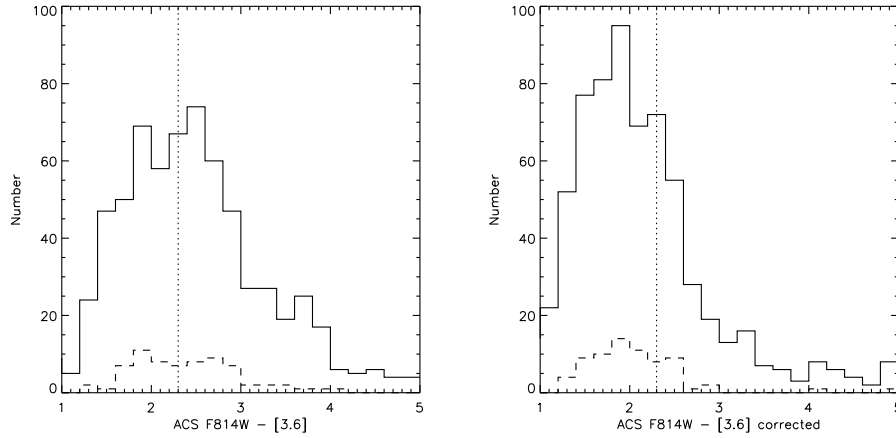


FIG. 5.— Histogram of colors of the star forming member galaxies (dashed) and all member galaxies (solid). At redshift one this color range is rest-frame B-K. The vertical dotted line shows roughly where the division between red and blue galaxies lies. The right figure shows the color distribution of the same samples where colors are corrected for extinction based on SED fitting and a Calzetti extinction law.

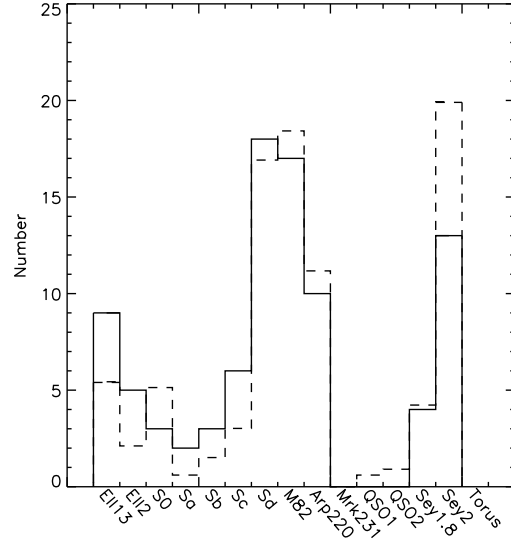


FIG. 6.— Best fit morphologies from HYPERZ SED fits. The solid line shows the member galaxies with $24\mu\text{m}$ detections and the dashed histogram is the normalized histogram of all field $24\mu\text{m}$ detections.

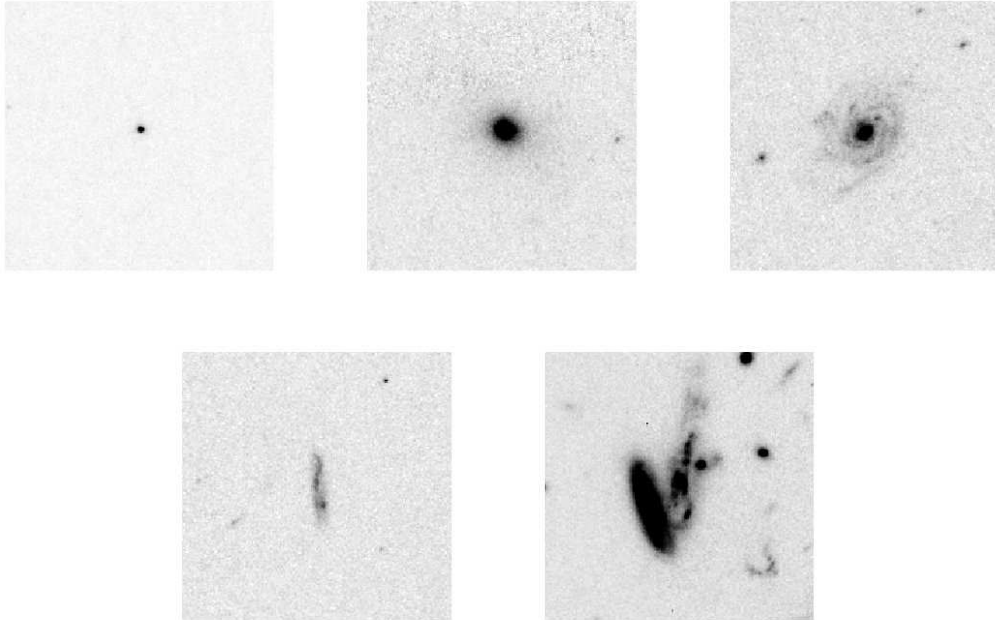


FIG. 7.— Examples from *HST* ACS F814W of each type in our morphological classification; Compact, Elliptical, Spiral, Irregular/Disk, and Irregular/Merger. All thumbnails are $10''$ on a side. The Irregular/Merger example comes from the center of cluster 2 and is our only ULIRG.

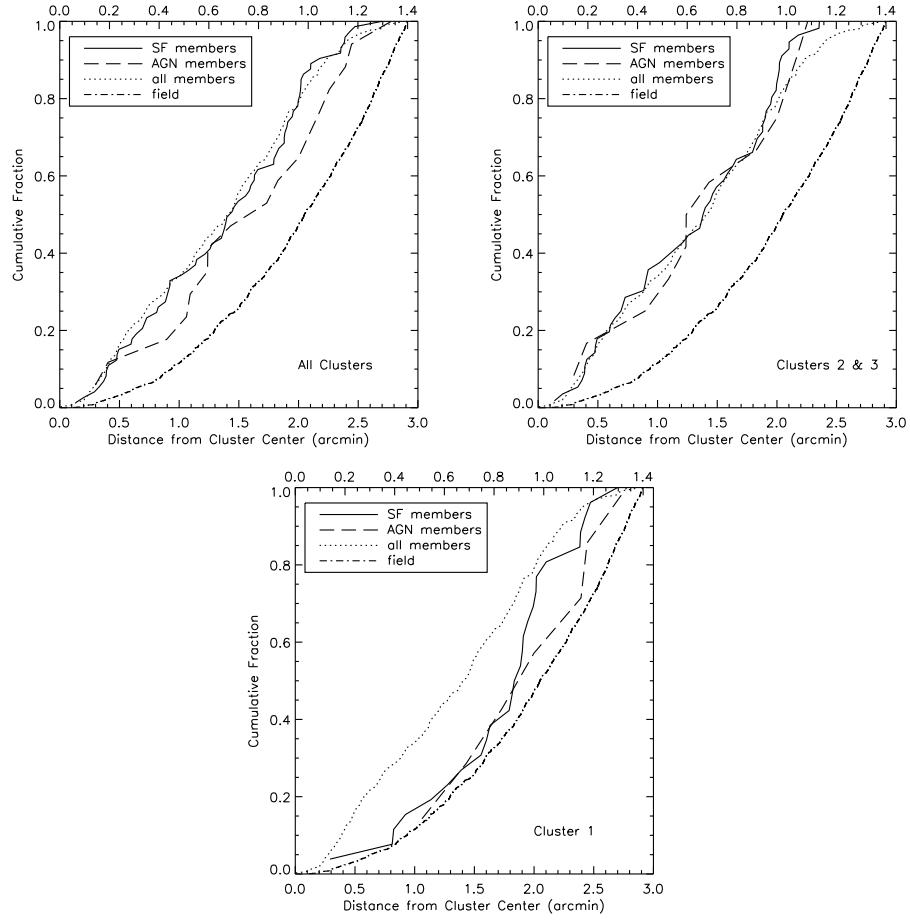


FIG. 8.— Cumulative distribution functions with distance from cluster center reported in arcminutes on the bottom axis and Mpc on the top axis. The solid, dashed, dotted, and dot-dashed lines represent the cluster star forming members, the cluster AGN members, all cluster members without MIPS flux or AGN SED shapes, and a field sample at redshift one respectively. *Top Left*: All three clusters combined; *Top Right*: Clusters 2 and 3 only; *Bottom*: Cluster 1 only.

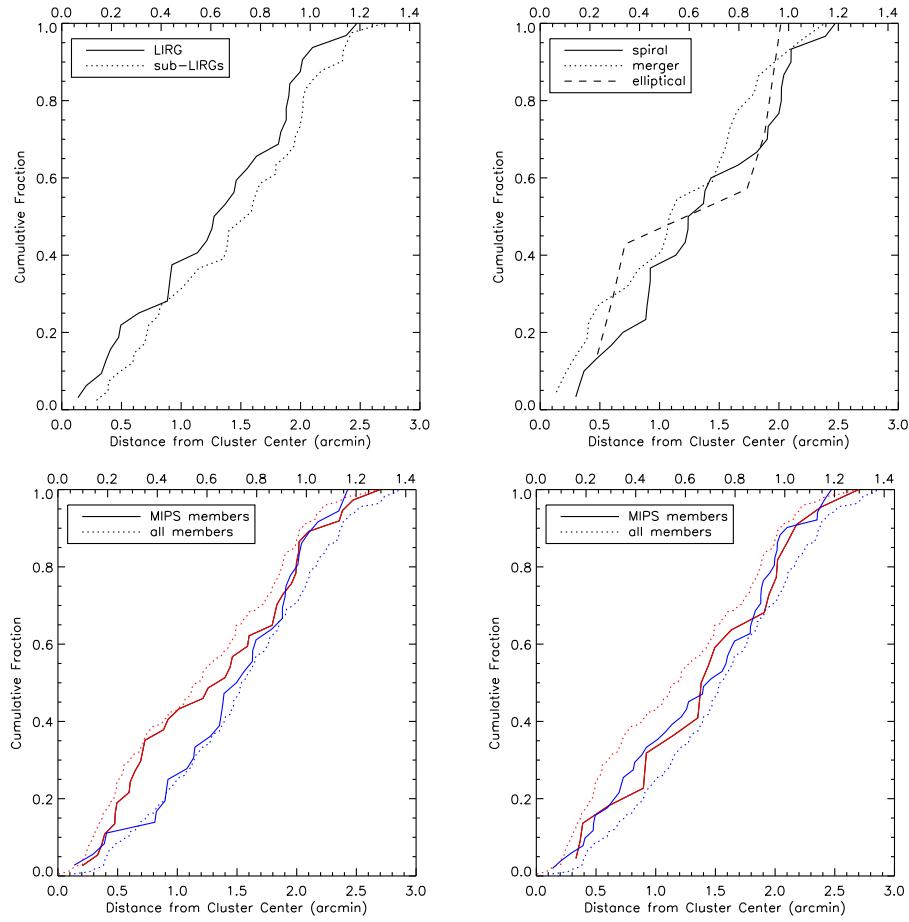


FIG. 9.— Cumulative distribution functions with distance from cluster center reported in arcminutes on the bottom axis and Mpc on the top axis. *Top left* Distribution split by infrared luminosity. LIRGS (including the lone ULIRG) are shown with the solid line, while sub-LIRGS are shown with the dotted line. *Top right* Distribution split by morphology into spirals (solid), ellipticals (dashed), and irregular/mergers (dotted). *Bottom left* Distribution split by color, uncorrected for reddening. The solid and dotted lines represent the cluster star forming members and all cluster members without MIPS flux or AGN SED shapes. The more concentrated set of solid and dotted (red) lines represent the red galaxies while the less concentrated (blue) set of lines show the blue galaxies. *Bottom right* Distribution split by reddening corrected color; same line definitions as the middle right plot.